Separation and Purification Technology 291 (2022) 120885

Contents lists available at ScienceDirect

Separation and Purification Technology

journal homepage: www.elsevier.com/locate/seppur

# Differentiating fouling on the membrane and on the spacer in low-pressure reverse-osmosis under high organic load using optical coherence tomography

Giorgio Pratofiorito [a,b,*], Harald Horn [a,b], Florencia Saravia [b]

[a] Engler-Bunte-Institut, Karlsruhe Institute of Technology (KIT), Water Chemistry and Water Technology, Engler-Bunte-Ring 9, 76131 Karlsruhe, Germany
[b] DVGW Research Center, Water Chemistry and Water Technology, Engler-Bunte-Ring 9a, 76131 Karlsruhe, Germany

ARTICLE INFO

*Keywords:*
Low-pressure reverse-osmosis
Biofouling
Optical coherence tomography (OCT)
Flat sheet membrane modules (FMM)
High organic load

ABSTRACT

The understanding of fouling mechanisms makes it possible to develop controlling strategies to optimize membrane performance. In this work, optical coherence tomography (OCT) was used for *in-situ* characterization of biomass occluding the feed channels of low-pressure reverse-osmosis membrane modules used to treat a feed stream with high organic load. A method for differentiating fouling formation on the membrane itself and on the spacer using two parameters (*ME,* for the membrane and *SP,* for the spacer) was developed. Pressure drop along the module and flux were measured at constant inlet pressure and then confronted with *ME* and *SP*. Pressure drop increased during the whole duration of the experiment. Flux declined by 30% after 25 days of filtration. Results clearly showed that biofilm grew on the feed spacer at first and on the membrane during the latter stage. Pressure drop seemed to be dominantly promoted by fouling accumulating on the spacer, while flux decline was correlated with fouling on the membrane surface. Interestingly, *ME* started increasing as *SP* reached its maximum, indicating a competition between the two types of fouling.

## 1. Introduction

In membrane separation processes both biofouling and organic fouling can lead to a severe permeability decline and even more affect the permeate quality. Therefore, the separation of low molecular weight organic compounds from solutions (hydrolysates) with a high fouling potential by the use of reverse-osmosis (RO) is challenging [1,2]. RO membranes are composite membranes, consisting of a thin polyamide active layer deposited on a supporting porous layer. The polyamide layer has a dense structure through which the solvent diffuses. It is generally assumed that dense membranes do not have pores. Herein, the dominant fouling mechanism for RO membranes is the formation of a fouling layer in the feed channel. The characteristics of this deposit (e.g. its porosity and thickness), which are influenced by the membrane properties and the composition of the treated solution, control the flux decline together with the operating conditions [3].

In spiral wound modules the bio/organic fouling load (mass of dried foulant material per unit surface area) is higher for the lead position module [3]. This effect is more pronounced when the concentration of organics in the feed is higher. However, in the last module, inorganic fouling/scaling is predominant mainly due to the higher concentration of salts toward the end of the feed channel.

Two key parameters for (bio)fouling control are flux and crossflow velocity [4]. High fluxes induce convective transport of bacteria and nutrient toward the membrane surface, favoring biofouling and thereby negatively affecting the channel pressure drop. However, crossflow velocity acts differently on the transmembrane pressure (TMP) and the channel pressure drop. TMP decreases with increasing crossflow velocity, while channel pressure drop is proportional to the square of the crossflow velocity. A higher cross flow velocity decreases concentration polarization of solutes, thereby slowering biofouling formation, which has a beneficial effect on TMP. Low crossflow velocities promote attachment and biological growth due to low shear forces. Shear stress also affects the biofilm structure, which can be fluffier or more compact if the fluid velocity in the channel is lower or higher, respectively [4]. Studies have investigated the interconnection between spacer geometries, shear stresses and biomass accumulation using different types of feed spacers (from column type to helical filaments spacers) [5,6,7,8].

* Corresponding author at: Engler-Bunte-Institut, Karlsruhe Institute of Technology (KIT), Water Chemistry and Water Technology, Engler-Bunte-Ring 9, 76131 Karlsruhe, Germany.
*E-mail address:* giorgio.pratofiorito@kit.edu (G. Pratofiorito).

https://doi.org/10.1016/j.seppur.2022.120885
Received 1 February 2022; Received in revised form 8 March 2022; Accepted 18 March 2022
Available online 25 March 2022

The smaller the clearance height (space between the spacer filament and the membrane surface), the higher the shear stress on the membrane, which in turns results into a faster attachment of biofouling. However, as filtration time progresses the fast growth of bacteria is enhanced in the central region of the rhombus, characterized by lower shear stresses and a stable hydrodynamic [6]. Also, regions where the flow field is more stable also showed less detachment of biomass and more favorable conditions for growth [6].

Several techniques have been used for the imaging of the fouling layer in feed channels: nuclear magnetic resonance (NMR), oxygen imaging with planar optodes, electrical impedance spectroscopy (EIS), and optical coherence tomography (OCT) [9–16]. Among them, OCT has proved to be a valuable technique to assess the distribution of biofilm and its structure at the mesoscale (from 100 μm up to 5 mm) [17,18]. This is due to the nondestructive nature of OCT and the fast image acquisition, that allow for *in-situ* real time characterization of the fouling layer. So far, several studies have been carried out to describe fouling of membrane systems and its negative effects on the process efficiency using OCT [10–16]. Once the OCT dataset is acquired, a major challenge is represented by image processing. Algorithms for image processing can be implemented using either already available plug-ins or custom-made scripts allowing for a more specific interpretation of the data.

In their study about biofouling in RO, West et al. investigated the biofilm development by means of OCT and the subsequent pressure drop along an RO flat sheet module under different organic loads of the feed and with different spacer geometries [11]. One of their main findings was that a small-meshed spacer promotes a faster biomass growth in comparison with a wide-meshed spacer. Nevertheless, the final pressure drops and biomass volumes associated to the different spacer geometries are comparable. A remarkable role on biofouling was played by the feed composition. Their study does not deliver any information about the distribution and the morphology of biomass, nor about surface coverage. To more deeply understand fouling mechanisms, spatially resolved biofilm quantification is needed. There are already some studies dealing with this aspect [12–14,19–21].

Bauer et al. investigated scaling in membrane distillation using OCT [12]. They analyzed the inorganic fouling layer, describing its structure with the help of image processing and demonstrated that it is possible to correlate macroscopic process parameters (i.e. flux and cumulated condensate volume) with local characteristics of the deposit. In a further research they assessed the impact of operating conditions – such as water matrix, temperature and air-gap/direct-contact configurations – on several scale parameters, concluding that the process can be optimized thanks to an accurate observation of the scale layer at a microscopic level [13].

Fortunato et al. performed OCT imaging during a 5 days experiment, in which they operated an ultrafiltration membrane fouling simulator, using tap water as feed [14]. Additionally, a nutrient solution was continuously dosed to trigger biomass formation. They quantified the biomass volume on the membrane, feed spacer and cover glass, finding that during the first 2 days the biomass accumulation in the module was low. Starting from the third day, biofilm attachment on the spacer was observed, accompanied by an increase of the pressure drop. The highest spreading of biofilm on the membrane occurred on the last two days of the experiment. The duration of the experiment was relatively short, due to fast biomass growth. A similar approach has not yet been applied to long term trials. Longer times of observation enable higher temporal resolution, therefore yielding more information about phenomena that might be overlooked when biomass growth occurs to fast.

The present study focuses on the development of a method for (bio) fouling quantification in spacer filled channels, with a view to reproducing fouling behavior in spiral wound modules. In contrast to previous works, the flat sheet membrane module (FMM) were operated with feed streams at high organic load. A synthetic solution simulating an anaerobic hydrolysate was fed to the units. The quantification of fouling was realized via OCT. The goal was to differentiate between the biofilm growing on the spacer filaments and the one growing directly on the membrane surface using microscopic parameters and to relate biofilm growth to macroscopic process variables. The pressure drop along the modules was measured as well as membrane permeability. An attempt has been made to understand whether the biofilm growing on the spacer or the one growing on the membrane (or both) dominates the flux decline at different stages of operation.

## 2. Materials and methods

### 2.1. Feed solution

Experiments were carried out using a model solution. The composition of the solution was formulated to simulate the hydrolysis product of pig manure and sugar beet at 55 °C and 1 bar. Table 1 displays the composition of the feed, which was mainly composed by acetate. The pH was 5.4 ± 0.1, the electrical conductivity was 17 ± 0.5 mS $cm^{-1}$ and the turbidity was 2.7 NTU. Hydrolysates with similar composition were produced by Kumanowska et al. and Ravi et al. [22,23].

### 2.2. Lab-scale LPRO setup

The experiment was performed on a LPRO system, equipped with two FMM arranged in parallel, in order to run the experiment in duplicate. Each module was provided with three optical windows (sapphire glass, 1″ diameter, 5 mm thickness, Thorlabs, Bergkirchen, Germany) facing the feed channel, allowing for the visualization of the fouling layer. To each window corresponded an imaging position (at 70 mm, 140 mm, and 210 mm from the inlet of the channel). XLE membrane sheets (FilmTec Dupont, Wilmington, DE, USA) were placed inside the modules. This membrane is a low energy polyamide thin-film composite membrane used for RO. A commercially available RO 28 mil woven spacer with a mesh of 3.5 mm was set in the feed channel. Due to the typical structure of the woven spacer, clearance height is not constant and for the 28 mil spacer amounts to 230–490 μm. A photograph of one module is displayed in Fig. 1a. The active surface of the sheet was 0.279 × 0.1 $m^2$ and the channel height was 0.7 mm.

Temperature was recorded by a sensor (2xPt100, Negele Messtechnick GmbH, Egg an der Günz, Germany) placed before the modules and kept constant by means of a thermostat. Pressure indicators (Cerabar PMP11, Endress + Hauser GmbH, Maulburg, Germany) were placed before and after the modules. The volumetric flow rates in the two parallel tracks on the retentate side was monitored by two magnetic inductive flowmeters (Picomag, Endress + Hauser GmbH, Maulburg, Germany). A diaphragm pump (G03, Verder, Haan, Germany) supplied both tracks with the feed. A simplified flow diagram of the setup can be seen in Fig. 1b. Permeate and concentrate were recirculated to the 5 L tank. The feed was renewed every day to limit bacterial growth inside the vessel.

### 2.3. Operational conditions

For 26 days the pressure before the modules was kept at 25 bar ± 0.5 bar while the temperature was 37 ± 1 °C. Experimental conditions were based on a previous work dealing with concentration of acetic acid [24].

**Table 1**
Feed composition.

| Component | g $L^{-1}$ |
|---|---|
| $CH_3COO^-$ | 16.9 |
| $Na^+$ | 2.8 |
| $K^+$ | 2.4 |
| $Ca^{++}$ | 1.4 |
| $Cl^-$ | 0.4 |
| $NH_4^+$ | 0.2 |

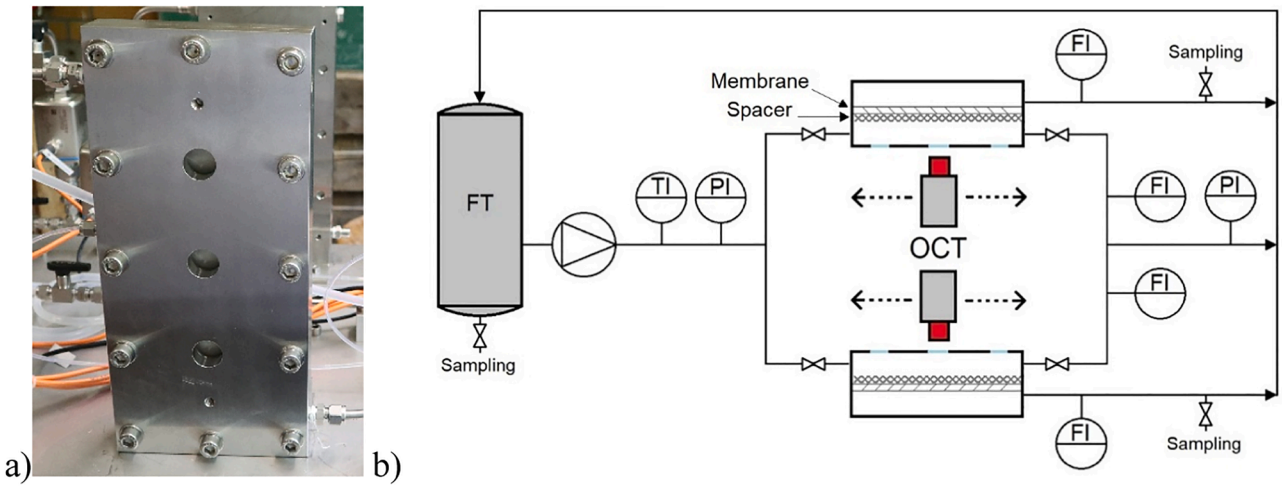


**Fig. 1.** Photograph of an FMM with optical windows (a) and schematic representation of the lab-scale LPRO setup (b). FT: feed tank; TI: temperature sensor; PI: pressure sensor; FI: flowmeter.

The average crossflow velocity inside the feed channel was 0.2 $ms^{-1}$ (Reynolds number, Re = 570), a typical value for spiral wound modules. Before starting the experiment, the system was run with deionized water at 10 bar for 3 h to for membrane pre-conditioning.

### 2.4. OCT and image processing

A GANYMEDE II spectral domain system (Thorlabs GmbH, Dachau, Germany) was used to perform OCT imaging. The OCT device was provided with an LSM04 objective lens (Thorlabs GmbH, Dachau, Germany). The A-scan acquisition rate was 36 kHz. The field of view (FOV) was set at 6 mm × 5 mm × 1.6 mm, in order to picture one rhombus of the spacer and the halves of the surrounding rhombuses. The axial resolution was 3.14 μm $voxel^{-1}$, whilst the resolution in the x-y plane was 8 μm $voxel^{-1}$. The refractive index was fixed at n = 1.33.

OCT C-scans consisted of a 3D image in which both the spacer and the membrane surface were represented. To separately analyze the information about the spacer and the membrane, an in-house ImageJ macro was written and run on Fiji (ImageJ version 2.1.0). The results of the image analysis on the three positions of the two parallel units were then averaged. Hereunder the processing steps for the membrane as well as for the spacer section of the picture are clarified.

#### 2.4.1. Image analysis of the membrane

The macro was tailored to every imaging position, since the spacer was placed differently inside the FOV depending on the acquisition spot. However, the spacer maintained the same location during the experiment, so that by every acquisition on the same spot at different times the topography of uncovered spacer and membrane was the same.

The raw C-scans were converted from 32-bit to 8-bit. To evaluate only the fouling formation on the membrane, a rhombus – corresponding to the region of the membrane that was not covered by the spacer – was cropped out of the raw image dataset (step A). The contour of the rhombus was defined by placing its vertexes 50 μm away from the corners of the spacer. In this way, the possible interference caused by the fouling formation on the spacer was excluded and only the portion of membrane uncovered by the spacer was analyzed.

A filter was applied and the contrast was enhanced (Step B). The image dataset was then flattened as described by Bauer et al. (Step C) [12]. This was necessary to align the bottom of the fouling layer on the same height inside the image, since the membrane was not perfectly flat. Thereafter, the contrast was enhanced and the image was binarized according to Yen et al. (Step D) [25]. The membrane area below the feed spacer was not considered in the calculation of *ME*. The spacer was indeed transparent and biofilm below the filaments could be seen, but the change of the refractive index at the spacer-liquid interface implied a shadowing effect with a subsequent distortion of the image. This can be clearly seen in the images provided in the supporting material. The membrane below the spacer appears to be displaced downwards. Image analysis in this region is likely to overestimate dimensions of objects. 2D images are provided in the supplementary material to show biological growth.

Fig. 2 depicts each step. It must be mentioned that the setting for the cropping and the processing of each spot were the same for the whole time series, allowing for a consistent treatment of the collected data.

#### 2.4.2. Image analysis of the spacer region

The spacer filaments do not have a constant section and present an irregular geometry. This makes the evaluation of 3D datasets more difficult than on the membrane, since the irregular geometry does not permit to write a macro that crops the image close enough to the spacer everywhere. For this reason, it was decided to analyze several B-scans (i.e. slices of the 3D stack) separately and to average the results to gain information about biofilm development on the spacer. Similarly, to the image processing of the membrane, the dataset had to be filtered, the contrast enhanced and the image binarized. Fig. 3 depicts the process of one B-scan yielding a binarized image of the cross-section of a spacer

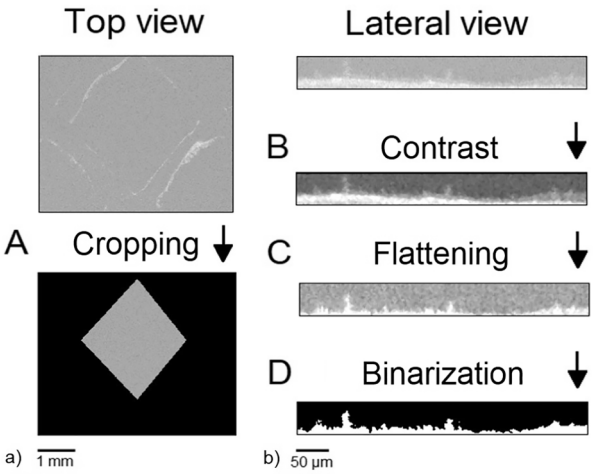


**Fig. 2.** Image processing steps for the membrane. Top view of a spacer rhombus (a) lateral view of the fouling layer on the membrane (b).

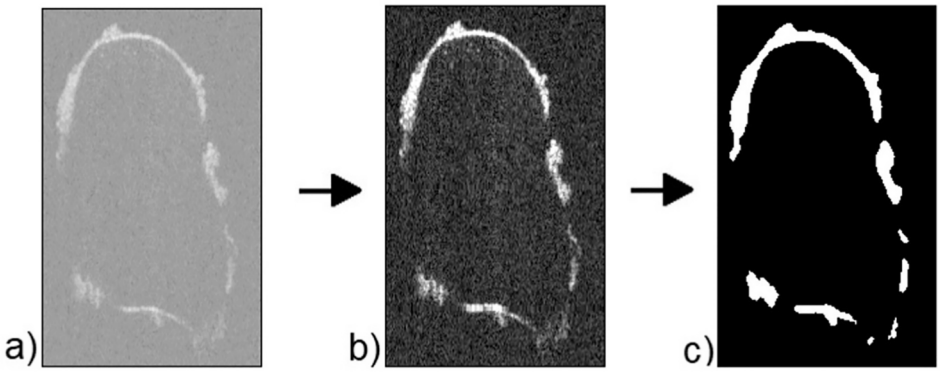


**Fig. 3.** Processing steps of a B-scan. The raw image dataset (a) is first filtered and the contrast is enhanced (b) and then the dataset is binarized (c).

filament.

#### 2.4.3. Development of parameters

To separately quantify the biofilm growing on the membrane (Fig. 2) and the one growing on the spacer (Fig. 3) the following parameters have been defined:

$$ME = \frac{V_{ME}}{S_{ME}} \tag{1}$$

$$SP = \frac{A_{SP}}{L_{SP}} \tag{2}$$

*ME* (μm) represents the average thickness of biofilm growing on the membrane. This applies under the assumption that biofilm growth on the membrane is quite homogeneous. $V_{ME}$ ($\mu m^3$) is the biovolume accumulated on the membrane and $S_{ME}$ ($\mu m^2$) the membrane area without spacer (area enclosed by the rhombus cropped from the image, Fig. 2). $V_{ME}$ is calculated by multiplying the white voxels of the processed C-scan times their size.

*SP* (μm) approximates the average thickness of the biofilm layer covering the spacer. $A_{SP}$ ($\mu m^2$) is the area obtained multiplying the number of white pixels in the processed B-scan of the spacer (Fig. 3c) times their size and represents the amount of fouling deposit on the spacer. $L_{SP}$ (μm) is the width of the spacer filament and is used to normalize $A_{SP}$, yielding a monodimensional parameter. $L_{SP}$ was calculated on the clean spacer with the built-in function "Straight" of Fiji for each B-scan, as the spacer did not have a constant cross-section, due to the irregular geometry. Precisely this irregular geometry did not make it possible, to implement the calculation of the spacer perimeter in the macro. The $L_{sp}$ values along the Y-direction are provided in the supplementary material.

To exclude the initial pressure drop provoked by the FMM itself and the tubing, the relative pressure drop was calculated:

$$\Delta p = p - p^0 \tag{3}$$

where $p$ is the pressure drop at a given time and $p^0$ is the initial pressure drop of 0.1 bar. Such a high initial value can be explained by the fact that the tube between the first pressure transducer and the FMM made a curve (Fig. 1b). This was the case also for the section between the FMM and the second transducer. Besides, the downstream sensor was placed after the valve for the setting of the flow velocity, resulting in an additional pressure drop.

## 3. Results and discussion

The FMM were run for a period of 26 days and three different positions were pictured daily by means of OCT on the modules. The focus of the work was to distinguish between (bio)fouling formation both on spacer and membrane surface. However, the separation performance of the membranes did not seem to be affected by biofouling. The retention of acetic acid fluctuated between 87% and 92% [24].

### 3.1. Biofilm development

The evolution of the two parameters is shown in Fig. 4. During the first 15 days the fouling formation on the membrane was very low and *ME* stayed below the OCT detection limit. Fouling started being more appreciable from the sixteenth day, showing an exponential increase. On the other hand, the build-up on the spacer was already evident from the beginning. Its rise was more linear than the one on the membrane and the average *SP* reached a maximum of 31 μm between day 16 and day 17. This value was maintained until the experiment was shut down. However, detachment and new attachment did also occur on the spacer during the final days. Some images are provided in the supplementary material to show the biofilm growth over time.

Fouling layer thickness strongly depends from nutrient concentration/water composition, shear stresses, and pressure. Despite the very high availability of carbon source and a cross flow velocity typical for spiral wound modules, the fouling layer was very thin due to high pressure. The final average height of the fouling layer on the membrane was about 11 μm. Fortunato et al. obtained an averaged thickness of fouling on an UF set-up of about 55 μm [19]. This value is five times higher than the one obtained in this study. Differences on the thickness of the fouling layer might be due to a) the presence of suspended solids in their feed (however smaller than 5 μm), leading to the formation of a cake and b) the pressure used in their study (1 bar), 25 times lower than the one used here, justifying the formation of a thicker layer. The higher pressure used in our study lead to the formation of a more compact layer. This layer can account for up to 80% of the filtration resistance [12]. The specific biomass resistance was calculated as described elsewhere [19] and amounted 3.3 μm $m^{-1}$. Another factor that might have increased the compactness of the fouling layer is the high concentration of $Ca^{2+}$ ions in the feed (35 mM). Pfaff et al. investigated the influence of calcium concentration in the supernatant (ranging from 1 mM to 15 mM) on the compactness of their biofilm [26]. They could correlate an increase of the concentration to a compacter structure of the layer, with a plateau at 8 mM. This fact has been explained with the higher crosslinking between negatively charged portions of extracellular polymeric substances (EPS). Both algal and bacterial biofilms showed this behavior. The resulting compactness explains the high hydraulic resistance experienced in our study. Another study showed that already a concentration of 0.5 mM of $Ca^{++}$ can promote the adsorption efficiency of EPS on an RO membrane, which lead to a lower flux [27].

Suwarno et al. performed an RO membrane autopsy followed by image acquisition via confocal laser scanning microscopy (CLSM). The biovolume of the material occluding the module was calculated using a commercially available software (IMARIS, Bitplane, Switzerland) and resulted to be higher than the one obtained herein (26.3 μm) [4]. This

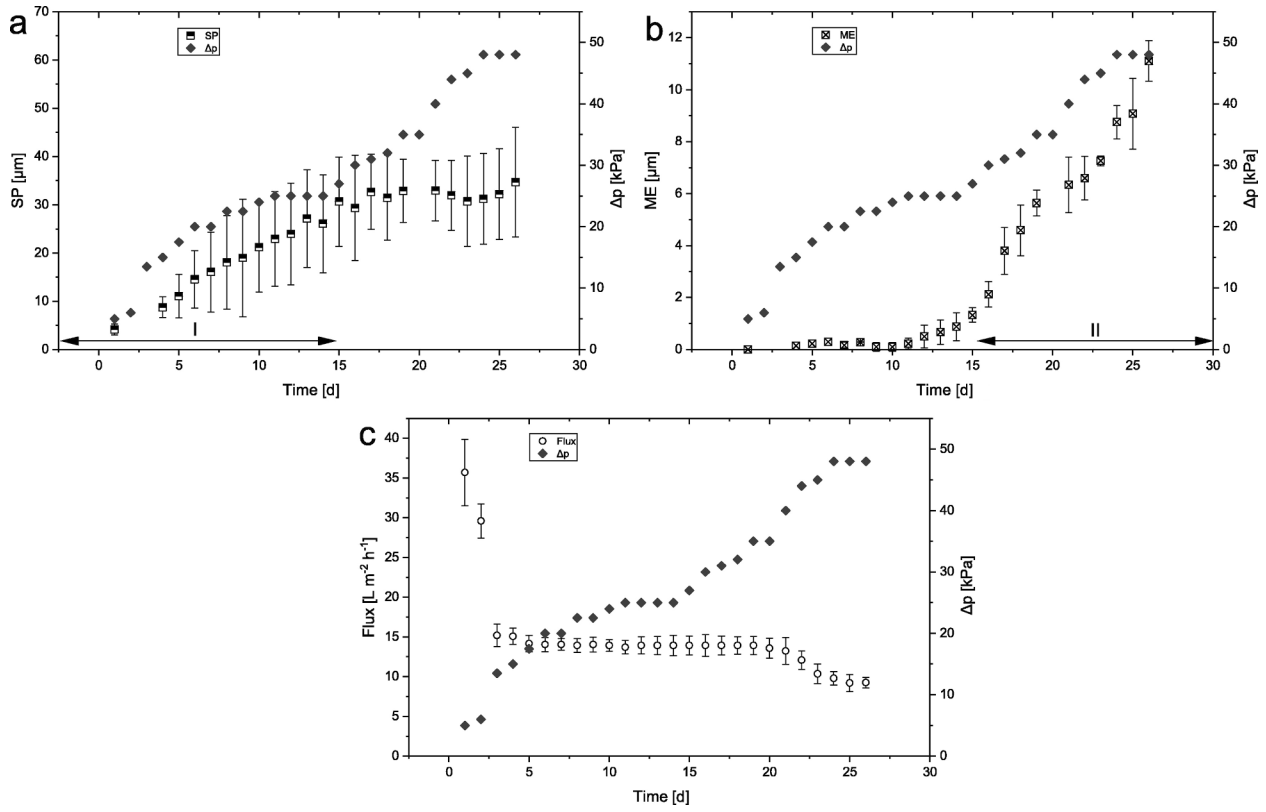


**Fig. 4.** Development of relative pressure drop together with spacer fouling (*SP*) (a), membrane fouling (*ME*) (b), and flux (c). The arrows show the phases in which pressure drop is governed by fouling on the spacer (I) and on the membrane (II).

can be on one hand because they operated their RO system at a pressure between 10 and 11 bar. On the other hand, the invasive nature of CLSM might have affected the accuracy of measurement. In fact, imaging was performed *ex-situ* and after staining. Removing the membrane from its place always implies the risk of modifying the structure of the biofilm and the release of pressure from 10 bar to ambient pressure might also have expanded it. This stresses the advantage of OCT as a noninvasive technique.

Although *SP* is scaled by the width of the spacer rather than its perimeter, it is reasonable to compare it with *ME*. Of course, it must not be a one-to-one comparison, since *SP* will be higher than *ME*, even when the amount of biomass per surface area is the same on the spacer and on the membrane. However, in this study *SP* appears to be two to three times higher than *ME*. Picioreanu et al. developed a three-dimensional computational approach to describe biomass attachment in feed channels [28]. One of their findings was that shear stress is higher on the membrane than on the spacer filaments because of the acceleration imparted to the fluid in the narrow section between the filament and the membrane surface. This might explain the difference between *ME* and *SP*. The values of *SP* are close to the "specific biovolume" obtained by Fortunato et al. with OCT [19]. Differences between the results of this and their study can be due to the different algorithm used for image analysis (filter, thresholding, etc.), different resolution of the image acquisition as well as to the specific operating conditions. On the other hand, the degree of biofouling on the spacer filaments obtained by Suwarno et al. is significantly lower (around 7 µm), probably due to the lower nutrient concentration of their feed solution (6.5 mg $L^{-1}$ total organic carbon, TOC) and the shorter duration of the experiment (10 days) [3].

As for the distribution of biomass on the membrane over the module length, in this work, no difference between the inlet and the distal positions could be detected. Apparently, the limited length of the module did not allow for diversification of the fouling layer. However, against expectations, the spacer of the terminal position had approximately 50% more biofilm compared to the lead and the central positions. It can be suggested that fragments of detached biomass were dragged by the current and accumulated on the spacer in the end section of the membrane module. This discrepancy is the cause of the big standard deviation reported in the graph (Fig. 4a).

### 3.2. Flux decline and feed channel pressure drop increase

The flux was continuously monitored over the duration of the experiment and the inlet pressure was kept constant. By measuring the outlet pressure, it was possible to determine the pressure drop along the module. Fig. 4c depicts the trends of the flux (average of the two parallel units) and the pressure drop. During the first two days of operation, flux decreased sharply, due to membrane compaction and the conditioning of the membrane by the feed. Preliminary experiments showed similar times for membrane compaction. Afterwards, it set to a stable value of 14 L $m^{-2}$ $h^{-1}$, which stayed stable until day 21. The experiment was concluded when flux decreased below 70% of the stable value.

The relative pressure drop in the feed channel increased almost constantly, indicating that the fouling on the spacer represents the main resistance to the flow in the channel. This is in accordance with previous simulations [26]. However, after day 15, Δp built up more rapidly, suggesting that also the fouling accumulating on the membrane played a role in the pressure drop. Looking at Fig. 4a and b, one notices that the pressure drop is governed by fouling on the spacer at first (phase I). However, from day 15 (phase II) the material accumulating on the membrane also contributes to the pressure drop. Given the low average height reached by the fouling layer on the membrane compared to the feed channel height (approx. 1%), it is unlikely that this fraction of fouling caused a substantial reduction of the cross section. It is more reasonable to think that, if it contributed at all to the pressure drop increase, this was rather due to the clogging of the narrow spaces between

the filaments and the membrane. We conclude therefore that the impediment of flow would then be localized in these regions and the distributed effect of fouling on "free membrane" (far from the spacer) would be neglectable. This conclusion is supported by the findings of Picioreanu et al. [28].

The total Δp divided by the time span (Δt) in which it is built up gives the rate of pressure drop increase ($\Delta p\ \Delta t^{-1}$). The rate observed in this study (1.8 kPa $day^{-1}$) was higher than the one reported by Suwarno et al. [3]. Spacer fouling is the main responsible for channel pressure drop. As discussed in section 3.1, in this study the fouling of the spacer was higher than the one found by Suwarno et al., suggesting that the different feed composition triggered a more severe pressure drop.

The maximum pressure drop normalized by the module length can also be used to compare results from different studies. The one obtained in this work (845 mbar $m^{-1}$) is close to what have already been reported elsewhere [19]. This might be explained by the similarity of the two used systems.

Interestingly, the pressure drop within the feed channel did not seem to affect flux. The inlet pressure was so high (2500 kPa) that the flux did not substantially suffer from the pressure drop increase, even considering the highest value of 50 kPa, accounting for only 2% of the inlet pressure. Reasonably, a longer module would have shown a higher deterioration of permeability owed to pressure drop. A typical spiral wound module is 1 m long, which would correspond to a pressure drop of 90 kPa. This holds under the assumption that the energy losses experienced herein can be directly upscaled solely according to the length and will not be exacerbated by the wider channel of a spiral wound module (typically 2.6 m of channel width) and by the cylindric geometry.

### 3.3. Surface coverage distribution

The topographic height maps of a representative membrane area are shown in Fig. 5. From day 10 fouling starts developing significantly, although only after day 16 a more uniform surface coverage is reached. This is confirmed by Fig. 6, revealing a rise in surface coverage around the same date. However, this descriptor is limited to the OCT resolution. This means that the interpretation of the results must take into account the possibility of a thinner foulant layer that could not be detected by the device. The fact that fouling starts accumulating again on the membrane once the attachment on the spacer has stopped is remarkable and suggests that from this point the deposition on the membrane surface is dominant. However, a direct correlation between surface coverage and flux decline could not be found, supposedly because a very thin layer is not sufficient to drastically hinder permeation. Together with the surface coverage, the average fouling thickness must be sufficiently high

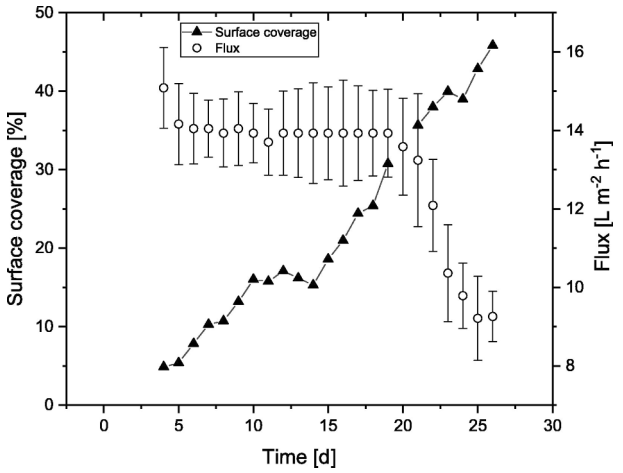


**Fig. 6.** Flux profile and surface coverage of a representative portion of membrane in the terminal region of a FMM.

before the final abrupt permeability drop occurs. This happens short after *SP* has reached its maximum. This appears to be the most convenient moment to start the cleaning, since the permeability drops within the very next days.

By comparing Fig. 4b with Fig. 6, it can be seen that surface coverage increases even before *ME*. This means that fouling distributes irregularly over the membrane at first, joining together in a thin film later on. Then the film builds up and vertical growth occurs only after a more or less uniform layer has already established. This underlines the importance of comparing different parameters describing biofilm structure (in this case *ME* and surface coverage). We speculate therefore that *ME* can be more easily related to the reduction of permeability than surface coverage, being a more useful key parameter for the prediction of membrane performance.

The possibility that a thin biofilm layer can still allow a high flux has already been proved [23]. Even with a thickness of 15 μm the permeability can remain essentially unaltered, being almost insensitive to the fouling layer. But again, given the high pressure used in this study, the compactness of the biofilm also plays a role. Accordingly, the height, at which permeability is affected, sinks to 7 μm. On the other hand, for scaling (where the inorganic material shows a higher hydraulic resistance than that of biofoulants) surface coverage can already be correlated with the deterioration of the membrane performance [14].

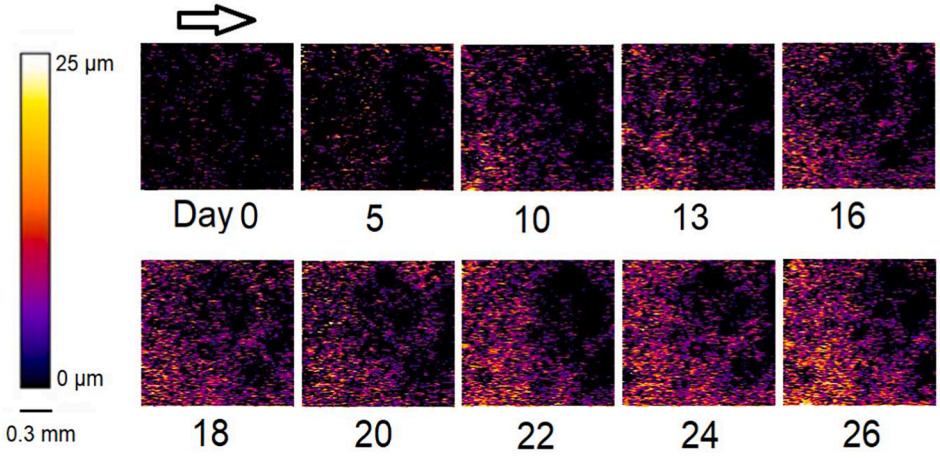


**Fig. 5.** Height maps of the biofilm pictured on the membrane. The arrow represents the flow direction. On the left, the calibration bar for the color linked depth code.

## 4. Conclusions

A method for biofouling differentiation in feed channels was presented, demonstrating that OCT is a powerful tool to predict both pressure drop in the feed channel and flux decline. The parameters *SP* and *ME* were particularly helpful to represent values for differentiating the biofouling. *ME* is a more relevant indicator for flux decline than surface coverage, confirming that the solution can permeate through the thin biofilm layer (in the order of few μm) without much hindrance. Flux appeared to decline after a certain *ME* value was reached. This happened after three weeks of operation, proving that long term operability under high organic load is possible.

In accordance with previous studies, fouling/biofouling grew on the feed spacer during the first stage of operation. Subsequently, a competition between membrane and spacer fouling appeared, followed by the stabilization of the amount of foulant on the spacer and an increase in the membrane surface coverage. Pressure drop increased during a first phase due to fouling on the spacer, whereas membrane fouling contributed only afterward. Therefore, cleaning cycles should be programmed before attachment on the spacer reaches its maximum (and stabilizes to a plateau), avoiding further deposition directly on the membrane surface. In this study, the maximum *SP* was reached at day 16, four days before drastic flux decline was detected.

## CRediT authorship contribution statement

**Giorgio Pratofiorito:** Conceptualization, Methodology, Software, Validation, Investigation, Data curation, Writing – original draft, Writing – review & editing, Visualization, Project administration. **Harald Horn:** Methodology, Validation, Resources, Data curation, Writing – review & editing, Visualization, Supervision, Project administration, Funding acquisition. **Florencia Saravia:** Conceptualization, Methodology, Validation, Resources, Data curation, Writing – review & editing, Visualization, Supervision, Project administration, Funding acquisition.

## Declaration of Competing Interest

The authors declare that they have no known competing financial interests or personal relationships that could have appeared to influence the work reported in this paper.

*Acknowledgements*

The authors thank the coworkers of the EBI workshop for the changes made to the plant and Dr. Annika Bauer and Dr. Michael Wagner for sharing their knowledge about image processing. The State Institute of Agricultural Engineering and Bioenergy, University of Hohenheim, Germany, is acknowledged for providing the hydrolysate.

*Funding*

This work was supported by the Federal Ministry of Education and Research (BMBF, Germany), in the framework of the project "Pro-BioLNG – *Biomethan für Industrie und Verkehr mittels innovativer Prozesskette erzeugen*" (Grant number 03SF0578B).

## Appendix A. Supplementary material

Supplementary data to this article can be found online at https://doi.org/10.1016/j.seppur.2022.120885.

## References

[1] T. Jänisch, S. Reinhardt, U. Pohsner, S. Böringer, R. Bolduan, J. Steinbrenner, H. Oechsner, Separation of volatile fatty acids from biogas plant hydrolysates, Sep. Purif. Technol. 223 (2019) 264–273, https://doi.org/10.1016/j.seppur.2019.04.066.

[2] Á. Bóna, P. Bakonyi, I. Galambos, K. Bélafi-Bakó, N. Nemestóthy, Separation of volatile fatty acids from model anaerobic effuents using various membrane technologies, Membranes 10 (2020) 252, https://doi.org/10.3390/membranes10100252.

[3] M. Tariq Khana, M. Busch, V. Garcia Molina, A.H. Emwas, C. Aubry, J.P. Croue, How different is the composition of the fouling layer of wastewater reuse and seawater desalination RO membranes? Water Res. 59 (2014) 271–282, https://doi.org/10.1016/j.watres.2014.04.020.

[4] S.R. Suwarno, X. Chen, T.H. Chong, D. McDougald, Y. Cohen, S.A. Rice, A.G. Fane, Biofouling in reverse osmosis processes: The roles of flux, crossflow velocity and concentration polarization in biofilm development, J. Membr. Sci. 467 (2014) 116–125, https://doi.org/10.1016/j.memsci.2014.04.052.

[5] S.M. Ali, A. Qamar, S. Kerdi, S. Phuntsho, J.S. Vrouwenvelder, N. Ghaffour, H. K. Shon, Energy efficient 3D printed column type feed spacer for membrane filtration, Water Res. 164 (2019), 114961, https://doi.org/10.1016/j.watres.2019.114961.

[6] S. Kerdi, A. Qamar, J.S. Vrouwenvelder, N. Ghaffour, Effect of localized hydrodynamics on biofilm attachment and growth in a cross-flow filtration channel, Water Res. 188 (2021), 116502, https://doi.org/10.1016/j.watres.2020.116502.

[7] S. Kerdi, A. Qamar, A. Alpatova, J.S. Vrouwenvelder, N. Ghaffour, Membrane filtration performance enhancement and biofouling mitigation using symmetric spacers with helical filaments, Desalination 484 (2020), 114454, https://doi.org/10.1016/j.desal.2020.114454.

[8] S. Kerdi, A. Qamar, J.S. Vrouwenvelder, N. Ghaffour, Fouling resilient perforated feed spacers for membrane filtration, Water Res. 140 (2018) 211–219, https://doi.org/10.1016/j.watres.2018.04.049.

[9] N.M. Farhat, M. Staal, S. Sz, M.C.M.V. Bucs, J.S.V. Loosdrecht, Spatial heterogeneity of biofouling under different cross-flow velocities in reverse osmosis membrane systems, J. Membr. Sci. 520 (2016) 964–971, https://doi.org/10.1016/j.memsci.2016.08.065.

[10] W. Li, X. Liu, Y.N. Wang, T.H. Chong, C.Y. Tang, A.G. Fane, Analyzing the evolution of membrane fouling via a novel method based on 3D optical coherence tomography imaging, Environ. Sci. Technol. 50 (13) (2016) 6930–6939, https://doi.org/10.1021/acs.est.6b00418.

[11] S. West, M. Wagner, C. Engelke, H. Horn, Optical coherence tomography for the in situ three-dimensional visualization and quantification of feed spacer channel fouling in reverse osmosis membrane modules, J. Membr. Sci. 498 (2016) 345–352, https://doi.org/10.1016/j.memsci.2015.09.047.

[12] A. Bauer, M. Wagner, F. Saravia, S. Bartl, V. Hilgenfeldt, H. Horn, In-situ monitoring and quantification of fouling development in membrane distillation by means of optical coherence tomography, J. Membr. Sci. 577 (2019) 145–152, https://doi.org/10.1016/j.memsci.2019.02.006.

[13] A. Bauer, M. Wagner, H. Horn, F. Saravia, Operation conditions affecting scale formation in membrane distillation – An in situ scale study based on optical coherence tomography, J. Membr. Sci. 623 (2021), 118989, https://doi.org/10.1016/j.memsci.2020.118989.

[14] L. Fortunato, S. Bucs, R. Valladares Linares, C. Cali, J.S. Vrouwenvelder, T. Leiknes, Spatially-resolved in-situ quantification of biofouling using optical coherence tomography (OCT) and 3D image analysis in a spacer filled channel, J. Membr. Sci. 524 (2017) 673–681, https://doi.org/10.1016/j.memsci.2016.11.052.

[15] S. Hube, J. Wang, L.N. Sim, T.H. Chong, B. Wu, Direct membrane filtration of municipal wastewater: Linking periodical physical cleaning with fouling mechanisms, Sep. Purif. Technol. 259 (2021), 118125, https://doi.org/10.1016/j.seppur.2020.118125.

[16] Y. Wanga, L. Fortunato, S. Jeong, T. Leiknes, Gravity-driven membrane system for secondary wastewater effluent treatment: Filtration performance and fouling characterization, Sep. Purif. Technol. 184 (2017) 26–33, https://doi.org/10.1016/j.seppur.2017.04.027.

[17] R. Valladares Linares, L. Fortunato, N.M. Farhat, S.S. Bucs, M. Staal, E. O. Fridjonsson, M.L. Johns, J.S. Vrouwenvelder, T. Leiknes, Mini-review: novel non-destructive in situ biofilmcharacterization techniques in membrane systems, Desalin. Water Treat. 57 (2016) 48–49, https://doi.org/10.1080/19443994.2016.1180483.

[18] M. Wagner, D. Taherzadeh, C. Haisch, H. Horn, Investigation of the mesoscale structure and volumetric features of biofilms using optical coherence tomography, Biotechnol. Bioeng. 107 (2010) 844–853, https://doi.org/10.1002/bit.22864.

[19] L. Fortunato, L. Ranieri, V. Naddeo, T. Leiknes, Fouling control in a gravity-driven membrane (GDM) bioreactor treating primary wastewater by using relaxation and/or air scouring, J. Membr. Sci. 610 (2020), 118261, https://doi.org/10.1016/j.memsci.2020.118261.

[20] L. Fortunato, N. Pathak, Z. UrRehman, H. Shon, T. Leiknes, Real-time monitoring of membrane fouling development during early stages of activated sludge membrane bioreactor operation, Process Saf. Environ. Prot. 120 (2018) 313–320, https://doi.org/10.1016/j.psep.2018.09.022.

[21] L. Fortunato, S. Jeong, T. Leiknes, Time-resolved monitoring of biofouling development on a flat sheet membrane using optical coherence tomography, Sci. Rep. 7 (2017) 1, https://doi.org/10.1038/s41598-017-00051-9.

[22] E. Kumanowska, M.U. Saldaña, S. Zielonka, H. Oechsner, Two-stage anaerobic digestion of sugar beet silage: The effect of the pH-value on process parameters and process efficiency, Bioresour. Technol. 245 (2017) 876–883, https://doi.org/10.1016/j.biortech.2017.09.011.

[23] P.P. Ravi, W. Merkle, M. Tuczinski, F. Saravia, H. Horn, A. Lemmer, Integration of membrane filtration in two-stage anaerobic digestion system: Specific methane yield potentials of hydrolysate and permeate, Bioresour. Technol. 275 (2018) 138–144, https://doi.org/10.1016/j.biortech.2017.09.011.

[24] G. Pratofiorito, H. Horn, F. Saravia, Impact of the recovery on concentrating acetic acid with low-pressure reverse-osmosis membranes, Membranes 11 (10) (2021) 742, https://doi.org/10.3390/membranes11100742.
[25] J.C. Yen, F.J. Chang, S. Chang, A new criterion for automatic multilevel thresholding, IEEE Trans. Image Process. 4 (1995) 370–378, https://doi.org/10.1109/83.366472.
[26] N.-M. Pfaff, J.M. Kleijn, M.C.M. van Loosdrecht, A.J.B. Kemperman, Formation and ripening of alginate-like exopolymer gel layers during and after membrane filtration, Water Res. 195 (2021) 116959, https://doi.org/10.1016/j.watres.2021.116959.
[27] M. Herzberg, S. Kang, M. Elimelech, Role of extracellular polymeric substances (EPS) in biofouling of reverse osmosis membranes, Environ. Sci. Technol. 43 (2009) 4393–4398, https://doi.org/10.1021/es900087j.
[28] C. Picioreanu, J.S. Vrouwenvelder, M.C.M. van Loosdrecht, Three-dimensional modeling of biofouling and fluid dynamics in feed spacer channels of membrane devices, J. Membr. Sci. 345 (2009) 340–354, https://doi.org/10.1016/j.memsci.2009.09.024.